

Valley-contrasting physics in a two-dimensional $p_{x,y}$ -orbital honeycomb lattice

Yuanyuan Wang, Chengwang Niu , Baibiao Huang, Ying Dai,* and Wei Wei*

School of Physics, State Key Laboratory of Crystal Materials, Shandong University, 250100 Jinan, China

 (Received 24 August 2021; revised 18 January 2022; accepted 31 January 2022; published 22 February 2022)

In valley physics, large spin-orbit coupling (SOC) is the key, which is however rather weak for many materials with two-dimensional (2D) hexagonal honeycomb lattice. In contrast to conventional materials such as graphene with active p_z orbitals, we proposed that large SOC splitting could be realized in $p_{x,y}$ -orbitals active honeycomb lattice, i.e., the XYH lattice. In particular, our model analysis confirmed that dynamically and magnetically induced valley polarizations are experimentally accessible. In accordance to the first-principles calculation and many-body perturbation theory, quaternary-layer BiSbC_3 proves our proposed physics, with extremely large SOC splitting of 567.9 meV, excitonic energy difference of 496 meV for characteristic A and B excitons, and valley polarization of 168.7 meV by V doping.

DOI: [10.1103/PhysRevB.105.075421](https://doi.org/10.1103/PhysRevB.105.075421)

I. INTRODUCTION

In the past few years, the valley degree of freedom has come to the front in fundamental physics and has been recognized to be at the center of the unprecedented valleytronics [1–3]. In comparison to the progress in spintronics, however, advances in valleytronics are modest, which is mainly due to the lack of material exemplification. It has already been known that lifting the degeneracy in K and K' valleys to generate distinguishable polarization is the precondition to manipulate the valley degree of freedom, and thus to observe the valley Hall effect or anomalous valley Hall effect. In this sense, materials such as doped h -BN and graphene are actually not satisfied due to the weak spin-orbit coupling (SOC) and small valley polarization [4,5]. It is fortunate that transition-metal dichalcogenides (TMDCs, e.g., MoS_2 and WS_2) characterized by inversion symmetry (P) breaking and strong SOC animate the valley physics [6–8]. In particular, in TMDCs in the two-dimensional (2D) limit there is opposite Berry curvature in K and K' valleys, and the valley-spin coupling (valley pseudospin), resulting in the valley-dependent helicity of optical transition [6,9,10]. In experiments, optical pumping with circularly polarized light is thus usually the dynamical way to detect the valley polarization [11–14].

In addition to 2D TMDCs, the currently most promising candidates for valleytronics are also extensively the hexagonal honeycomb lattices, with the p_z orbitals of group A elements and the d orbitals of transition metals predominantly contributing the frontier states. In some 2D honeycomb structures, cases with $p_{x,y}$ orbitals constituting the states near the Fermi level exist [15], which is referred to as $p_{x,y}$ -orbitals active honeycomb lattice (XYH lattice) in this work. As for the XYH lattices, topological physics and the strong orbital interactions leading to superconductivity and flat-band ferromagnetism were demonstrated [16–19], in spite of the dispersion in flat

bands caused by the non-negligible π -type hopping [20–22]. In contrast, for the XYH lattice the simultaneous band crossing at K/K' point is robust against this π -type hopping. On account of the extremely large SOC spin splitting caused by $p_{x,y}$ orbitals (discussed later), XYH lattices manifest themselves a great opportunity for the valley-contrasting physics. In this context, how to open energy gaps at the Dirac points and break the inversion symmetry turn out to be the barrier for XYH lattice for the valley physics.

In order to remove the barrier and transform the concept of XYH lattice-based valley physics into real materials, features of the Kagome lattice should also be considered. It is due to the phenomena that (1) p orbitals of the three inequivalent sites contribute to the parabolic energy dispersion relationship at high-symmetry K/K' point [23], while the threefold rotation symmetry leads to the decoupling between p_z and $p_{x,y}$ orbitals; (2) its parabolic band dispersion relationship near the K/K' point is similar to that of the XYH lattice. In the following, we will prove that combing honeycomb with Kagome (HK) lattices is an effective strategy to cause $p_{x,y}$ orbitals contributed valleys near Fermi level and keep the p_z orbitals away.

In this work, a general tight-binding (TB) model was used to illustrate how valleys are generated at the K and K' points of XYH lattice, and two feasible methods creating valley polarization were discussed. In particular, we revealed that the valley-contrasting Berry curvature and valley-dependent optical selection rule can be retained under time-reversal symmetry (T); in this case, the valley degree of freedom could be manipulated by optical pumping. On the other hand, intervalley energy degeneracy can be lifted if T is broken, e.g., by magnetic doping. In practice, quaternary-layer (QL) BiSbC_3 of HK lattice as a material realization consolidates our conclusion through the first-principles calculations and many-body perturbation theory. In regard to QL BiSbC_3 , our results reveal that the giant SOC splits the valence band into two subbands characterized by spin-valley locking; and the significant SOC spin splitting is addressed by the well-resolved characteristic

*Corresponding authors: daiy60@sdu.edu.cn; weiw@sdu.edu.cn

A and B bound excitons. In order to break T , V atom doping in QL BiSbC₃ was employed, which successfully removes the intervalley energy degeneracy with merit that impurity states are absent in the global band gap, causing significantly large valley polarization.

II. COMPUTATIONAL METHODS

In this work, the first-principles calculations were carried out with Perdew-Burke-Ernzerhof (PBE) functionals in the framework of generalized gradient approximation (GGA), as implemented in the Vienna *ab initio* simulation package (VASP) [24–26]. In order to avoid the interactions between nearest slabs, a 20 Å vacuum layer was added in the z direction. As for V d orbitals, GGA+U scheme was employed with $U = 3$ eV [27]. In electronic structure calculations, spin-orbit coupling (SOC) was incorporated, and the maximally localized Wannier functions were constructed using the WANNIER90 package [28]. On the basis of a $3 \times 3 \times 1$ supercell, phonon spectrum was calculated by using the PHONOPY code [29]. In order to obtain the correct excited-state properties and optical absorption spectra, scheme of GW approximation (G and W represent the single-particle Green's function and screened Coulomb interaction, respectively) and the Bethe-Salpeter equation (BSE) were used on the basis of *ab initio* many-body Green's function perturbation theory. In particular, DFT-PBE energies were corrected by one-shot G_0W_0 approximation to get the quasiparticle eigenvalues. In conjunction with the Quantum Espresso distribution, the GW+BSE calculations were performed by the YAMBO code [30,31]. In order to describe the large SOC effects well, Troullier-Martins norm-conserving fully relativistic pseudopotential was used for the plane wave functions [32]. In our calculations, the plane wave energy cutoff in the ground state was set to 60 Ry, and a $18 \times 18 \times 1$ k grid was used to obtain the quasiparticle energies. As for the self-energy and the dynamical dielectric screening, 300 bands were employed. In order to avoid the long-range interactions, a Coulomb cutoff of the screened potential was used in both G_0W_0 and BSE calculations. In the Bethe-Salpeter kernel, four highest valence bands and four lowest conduction bands were calculated. In our convergence tests, the number of bands and k points were sufficient, with the change in quasiparticle band gap and excitonic peaks in the BSE spectra being within 50 meV.

In order to estimate the thermodynamic stability of the QL BiSbC₃ with molecular formula Bi₂Sb₂C considered here, we estimated its bulk cohesive energy according to $E_{\text{coh}} = (E_{\text{tot}} - 2E_{\text{Bi}} - 2E_{\text{Sb}} - 6E_{\text{C}})/10$, where E_{tot} is the energy of the unit cell, $E_{\text{Bi/Sb}}$ and E_{C} are the energies of individual bismuth/antimony and carbon atoms, respectively. As for QL BiSbC₃, the calculated E_{coh} is -5.98 eV/atom, which is comparable to those of graphene, benzene and graphene nanoribbons, indicative of high thermodynamic stability.

III. RESULTS AND DISCUSSION

In Fig. 1(a), a typical XYH lattice with staggered sublattice is schematically shown, where a sixfold rotation can transform A sublattice to B sublattice and this system exhibits threefold

rotational symmetry. In case that $p_{x,y}$ orbitals are contributing to each lattice site, the Hamiltonian with only the staggered sublattice potential involved can be written as

$$H_0 = t_{\parallel} \sum_{\langle i,j \rangle} p_{\parallel,i}^{\dagger} p_{\parallel,j} - t_{\perp} \sum_{\langle i,j \rangle} p_{\perp,i}^{\dagger} p_{\perp,j} + \lambda \sum_i \eta_i p_i^{\dagger} p_i, \quad (1)$$

where t_{\parallel} , t_{\perp} and λ are the corresponding the strength of σ , π hopping, and staggered sublattice potential, respectively. $\delta_{1,2} = \pm 1/2\mathbf{e}_x + 1/(2\sqrt{3})\mathbf{e}_y$ and $\delta_3 = -1/\sqrt{3}\mathbf{e}_y$ are the vectors from A site to its three nearest neighboring B sites; $p_{\parallel,i} = (p_x\mathbf{e}_x + p_y\mathbf{e}_y)\delta_i$ and $p_{\perp,i} = (-p_x\mathbf{e}_y + p_y\mathbf{e}_x)\delta_i$ are p orbital projection parallel and perpendicular to the bond direction δ_i ($i = 1, 2, 3$), respectively; In Eq. (1), the first two terms represent the nearest-neighboring hopping, and the last term represents the staggered sublattice potential with $\eta_i = \pm 1$ and $p_i = p_{ix}\mathbf{e}_x + p_{iy}\mathbf{e}_y$ with i being the index for the A/B sublattice. In momentum space, to obtain the spectrum of the TB model a four-component spinor is given as $\{|p_{Ax}(\mathbf{k})\rangle, |p_{Ay}(\mathbf{k})\rangle, |p_{Bx}(\mathbf{k})\rangle, |p_{By}(\mathbf{k})\rangle\}^T$, with each component being the Fourier transformation of the $p_{x,y}$ orbitals on A or B site. As a result, the TB Hamiltonian $H_0(k_x, k_y)$ reads

$$H_0(k_x, k_y) = \begin{pmatrix} \lambda I & h(k_x, k_y) \\ h^{\dagger}(k_x, k_y) & -\lambda I \end{pmatrix}, \quad (2)$$

$$h(k_x, k_y) = \begin{pmatrix} (\frac{3}{4}t_{\parallel} + \frac{1}{4}t_{\perp})\alpha_+ + t_{\perp}\beta & \frac{\sqrt{3}}{4}(t_{\parallel} - t_{\perp})\alpha_- \\ \frac{\sqrt{3}}{4}(t_{\parallel} - t_{\perp})\alpha_- & (\frac{1}{4}t_{\parallel} + \frac{3}{4}t_{\perp})\alpha_+ + t_{\parallel}\beta \end{pmatrix}, \quad (3)$$

where $\alpha_{\pm} = e^{(-ik\cdot\delta_1)} \pm e^{(-ik\cdot\delta_2)}$, $\beta = e^{(-ik\cdot\delta_3)}$, and I is the 2×2 identity matrix.

The band dispersion relationship over the entire Brillouin zone [Fig. 1(b)] is obtained by diagonalizing the Hamiltonian matrix. As Fig. 1(c) shows, introducing staggered sublattice potential causes valleys appearing at the corner of the Brillouin zone, and the resultant inversion symmetry breaking is responsible for the valley-contrasting Berry curvature. It should be noted that the time reversal symmetry is kept after the introduction of staggered sublattice potential. In accordance to the Kubo formula [33], Berry curvature was calculated. As Fig. 1(d) shows, it particularly exhibits a characteristic odd function about the Γ point, and results from our TB model are consistent with theoretical analysis.

In general, large SOC splitting is indispensable for valleytronics, since the valley-spin coupling is basic for detecting and manipulating the valley degree of freedom. It is conclusive that for single-orbital (p_z) honeycomb lattices such as graphene, the on-site and the nearest-neighbor (NN) SOC are forbidden by symmetry constraint, and the SOC from the next-nearest-neighbor (NNN) second-order processes is however tiny [18]. It is of interest that the staggered sublattice potential in conjunction with frontier $p_{x,y}$ orbitals, which contribute to the band edge states, can enhance the SOC drastically; because the on-site SOC has nonzero matrix elements in $p_{x,y}$ orbitals constituted low-energy Hilbert subspace, which leads to large SOC spin splitting at K and K' points. In other words, the on-site SOC interactions for A ($|A \uparrow / \downarrow\rangle \rightarrow |A \uparrow / \downarrow\rangle$) and B ($|B \uparrow / \downarrow\rangle \rightarrow |B \uparrow / \downarrow\rangle$) sublattices are nonzero (with opposite signs for A and B

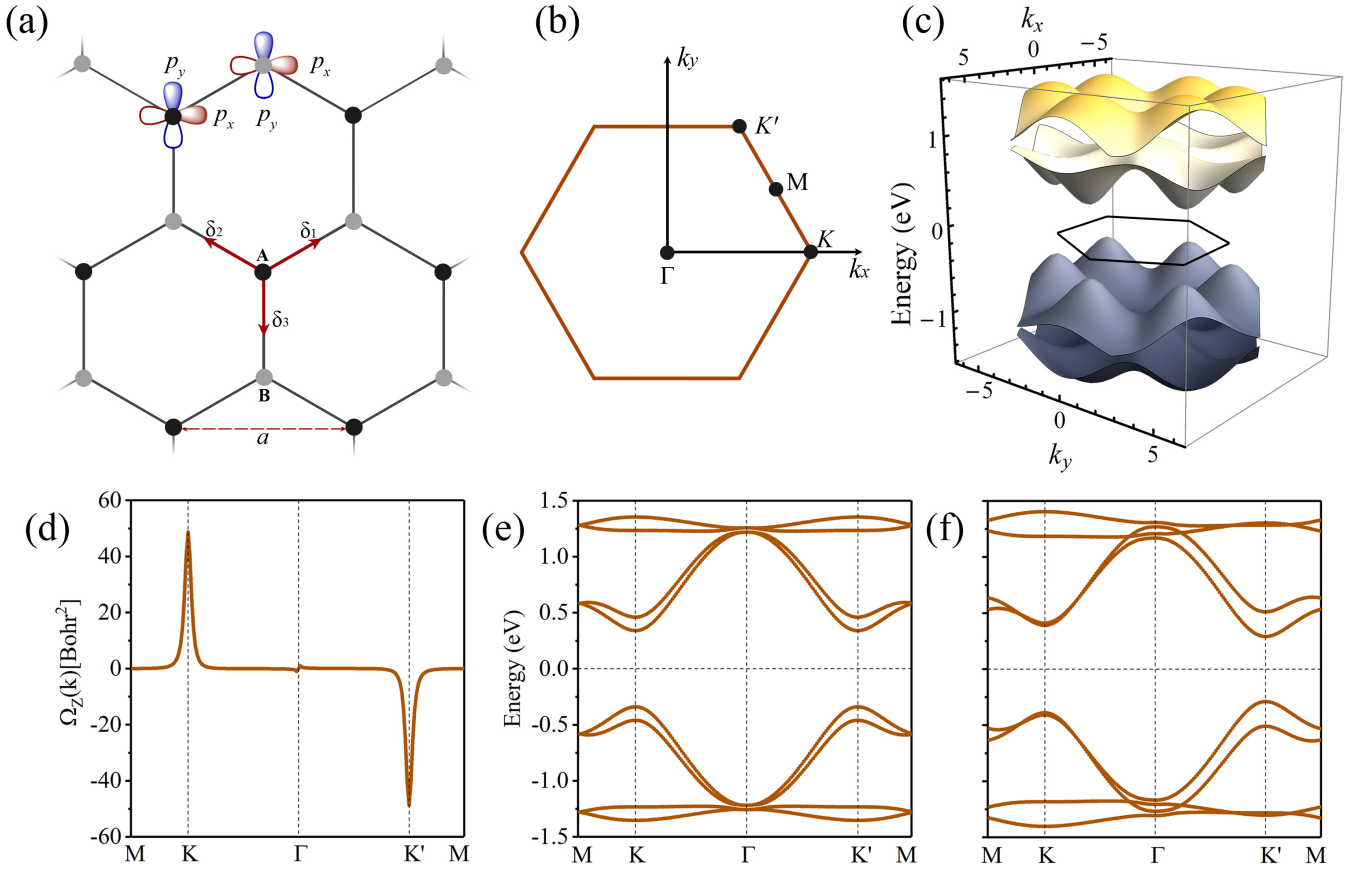


FIG. 1. (a) Sketch of the $p_{x,y}$ -orbitals honeycomb lattice with sublattice asymmetry, a and δ_i are the lattice constant and the length of the nearest neighbor bond, respectively. Without loss of generality, the convention $a = 1$ is adopted throughout the rest of this article. (b) Hexagonal Brillouin zone with edge length of $4\pi/3a$. (c) Energy dispersion in three dimensions, and (d) Berry curvature of $p_{x,y}$ -orbitals model in the presence of the π bonding t_{\perp} without considering the SOC effect. 2D band structure from model Hamiltonian (e) without and (f) with a uniform Zeeman field when SOC is considered. Parameters used are $\lambda = 0.4$, $t_{\perp} = 0.8$, $t_{\parallel} = -0.02$, $\gamma = 0.06$ and $\mu = 0.05$. t_{\parallel} and t_{\perp} are the corresponding σ - and π -hopping strengths, respectively. λ , γ , and μ represent the strength of staggered sublattice potential, SOC and Zeeman fields, respectively. The energy unit for these parameters is set to 1.

sublattices), and exhibit large strength due to the nonvanishing orbital angular momentum $l_z = \pm 1$ of the eigenstates $1/\sqrt{2}(p_x \pm ip_y)$ at the K/K' point [18,34]. In this case, Hamiltonian is rewritten based on the eight-component basis $\{|\uparrow, \downarrow\} \otimes \{|p_{Ax}(\mathbf{k})\}, |p_{Ay}(\mathbf{k})\}, |p_{Bx}(\mathbf{k})\}, |p_{By}(\mathbf{k})\}\}^T$, to account for the large influence on SOC:

$$H(\mathbf{k}) = \begin{pmatrix} \lambda I + \gamma \hat{s}_y & h(k_x, k_y) & 0 & 0 \\ h^\dagger(k_x, k_y) & -\lambda I + \gamma \hat{s}_y & 0 & 0 \\ 0 & 0 & \lambda I - \gamma \hat{s}_y & h(k_x, k_y) \\ 0 & 0 & h^\dagger(k_x, k_y) & -\lambda I - \gamma \hat{s}_y \end{pmatrix}, \quad (4)$$

where \hat{s} and γ are Pauli matrix and SOC strength, respectively. As shown in Fig. 1(e), evident SOC splitting occurs at K/K' point, which is crucial for the valley-spin coupling.

In accordance to the band structures from the tight-binding method, Wu *et al.* and Zhou *et al.* have demonstrated the possibility to achieve the multiple Hall effect in the honeycomb lattice of $p_{x,y}$ orbitals that exhibits topological nontrivial properties [21,22,35]. In a recent work, Zhou *et al.* exhibited how to realize high-density arrays of quantum spin-valley Hall kink states with spin-valley-momentum locking based on the XYH lattices [36]. In comparison to these proposed

models, in the present work both σ and π hopping are considered with $t_{\parallel} \ll t_{\perp}$, and the lattice potential is required to be larger than the strength of the intrinsic SOC, i.e., $\lambda > \gamma$. It is therefore verified that the honeycomb lattice with staggered sublattice potential together with the frontier $p_{x,y}$ orbitals can be used as a potential model for the study of nontrivial valley physics. In the following, possibility to realize valley Hall effect and anomalous valley Hall effect will be discussed.

In the language of group theory, optical selectivity of valley interband transitions have been discussed in consideration of the pure rotational group [9,11]. In accordance to the valley-dependent optical selection rule, the interband transition in K/K' valley couples exclusively to the σ_+/σ_- circularly polarized light for the case of transition metal d_{z^2} ($d_{x^2-y^2} \pm id_{xy}$) orbitals that dominate the conduction (valence) band [9,11], as well as for the band edges contributed fully by p_z orbitals in gapped graphene system [4]. It is still unclear, to the best of our knowledge, whether the valley-contrasting circularly polarized light selection rule is applicable for the XYH lattice with $p_{x,y}$ orbitals contributing the valleys. It is quite different from the systems mentioned above, for XYH lattice both sublattice and local $p_{x,y}$ atomic orbitals symmetries determine the

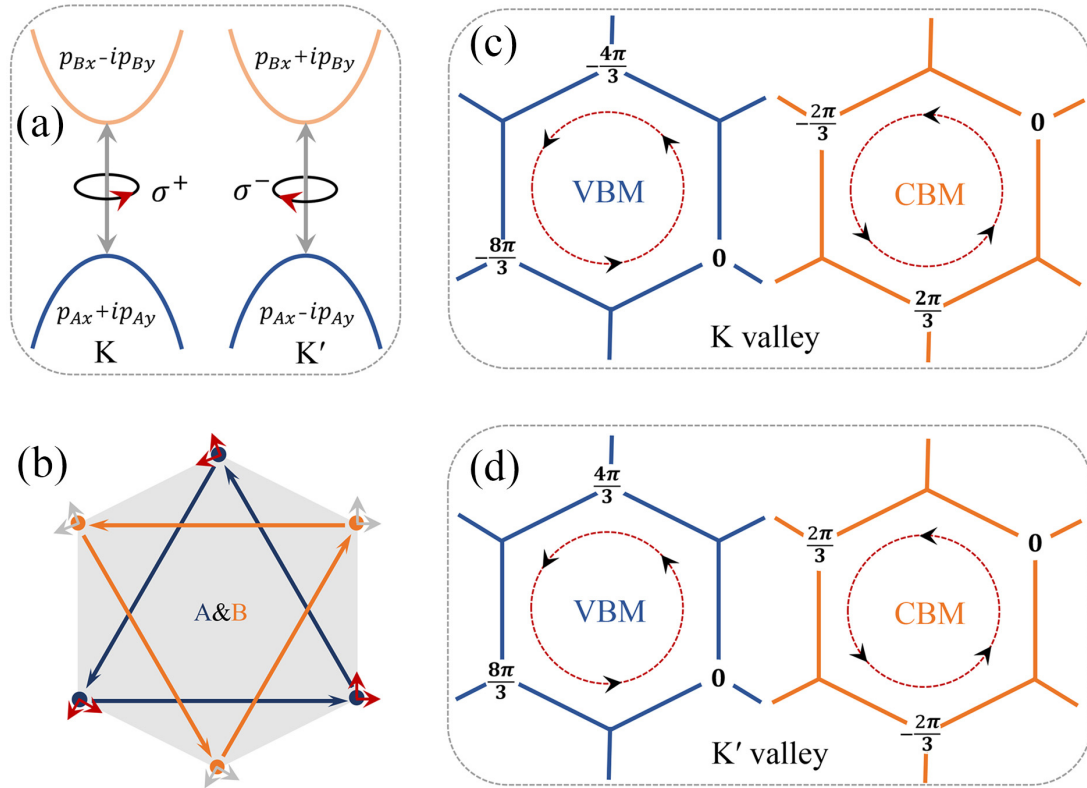


FIG. 2. (a) Valley-selective optical selection rules: σ_+/σ_- circularly polarized light couples only to band edge transitions in K/K' valley. (b) Schematic of phase winding in the XYH lattice that gives rise to the chiral optical selectivity, blue and yellow vectors represent the phase winding contribution from Bloch lattice phase, and red and gray axes indicate the rotation of local atomic coordinates that leads to the azimuth desynchronization, that is, the phase winding under a threefold rotation. Total phase winding of the Bloch function of valence and conduction bands in (c) K and (d) K' valley.

chiral absorptivity. As discussed in following, however, the feasible way proposed by Feng *et al.* [9,11] is still applicable for the valley optical selectivity in XYH lattice.

In consideration of the C_{3h} point group symmetry and lattice translational symmetry, see Fig. 2(a), a set of eigenstates $1/\sqrt{2}(p_{Ax} \pm ip_{Ay})$ and $1/\sqrt{2}(p_{Bx} \mp ip_{By})$ are, respectively, assigned for the valence band maximum (VBM) and conduction band minimum (CBM) at K/K' point, which spans a subspace. In essence, the optical selection rule is rooted in the phase winding of the Bloch states under rotational symmetry, threefold rotation symmetry (C_3) in our case. As illustrated in Fig. 2(b), the rotation associated phase winding shows two distinct contributions; the first one comes from the Bloch phase shift in stepping from one lattice site to the next (blue and yellow vectors), as in the case of gapped graphene [4]; the second phase factor arises from the desynchronization of the azimuthal phase (related to the magnetic quantum number), concomitant with the rotation of local atomic coordinates (red and gray axes). In consideration of σ_{\pm} pumping, which is correlated with the interband matrix element $P_{\pm} = \langle n', \mathbf{k} | \hat{p}_x \pm i\hat{p}_y | n, \mathbf{k} \rangle$ with n and n' being the Bloch states at crystal momentum \mathbf{k} , the selectivity may be derived by inspecting the effects of \hat{C}_3 on the matrix element. In this case, by inserting the operator \hat{C}_3 into P_{\pm} , the interband matrix element can be written as $P_{\pm} = \langle n', \mathbf{k} | \hat{C}_3^{-1} \hat{C}_3 (\hat{p}_x \pm i\hat{p}_y) \hat{C}_3^{-1} \hat{C}_3 | n, \mathbf{k} \rangle$. It gives rise to $\hat{C}_3 | n, \mathbf{k} \rangle =$

$\exp(i l_{nk} 2\pi/3) | n, \mathbf{k} \rangle$ once operating \hat{C}_3 on the eigenstates of C_3 rotational symmetry for K/K' valley, where the phase winding of the Bloch states is the sum of two terms $l_{nk} = l_L + l_M$. In particular, l_L and l_M arise from lattice phase winding of the Bloch phase factor $\exp(i\mathbf{k} \cdot \mathbf{r})$ and the local relative azimuthal phase of the atomic orbitals, respectively. It reads $\hat{C}_3 (\hat{p}_x \pm i\hat{p}_y) \hat{C}_3^{-1} = \exp[\mp i(2\pi/3)] (\hat{p}_x \pm i\hat{p}_y)$, and thus $P_{\pm} = \exp[-i(l_{n'k} - l_{nk} \pm 1)2\pi/3] P_{\pm}$. It follows $P_{\pm} = P_{\pm}$ and $P_{\mp} = \exp[\pm i(4\pi/3)] P_{\mp}$, when the modulo $(l_{n'k} - l_{nk}, 3) = \mp 1$. As a consequence, $P_{\mp} = 0$ and the vertical optical transitions at band gap are allowed exclusively by σ_{\pm} . In Figs. 2(c) and 2(d), the total phase windings for the VBM (CBM) in the K/K' valley are shown, respectively. It is therefore conclusive that valley-contrasting circularly polarized light selection rule is applicable for XYH lattice, as Fig. 2(a) shows.

In order to realize the anomalous valley Hall effect, on the other hand, the intervalley energy degeneracy should be lifted; a feasible strategy is to break the T by introducing ferromagnetic or antiferromagnetic order. In the case for the XYH lattice, ferromagnetic order is considered for the $H(\mathbf{k})$, and the Hamiltonian for Zeeman field effect can be represented as $H_{\text{ex}} = \mu \hat{s}_z \hat{\tau}_0 \hat{\sigma}_0$, where μ is the strength of Zeeman field and Pauli matrices \hat{s} , $\hat{\tau}$, and $\hat{\sigma}$ describe the spin, sublattice, and orbital degrees of freedom, respectively. In this case, the effective Hamiltonian for a ferromagnetic XYH lattice finds $H_{\text{eff}}(\mathbf{k}) = H(\mathbf{k}) + H_{\text{ex}}$. As Fig. 1(f) shows, when introducing

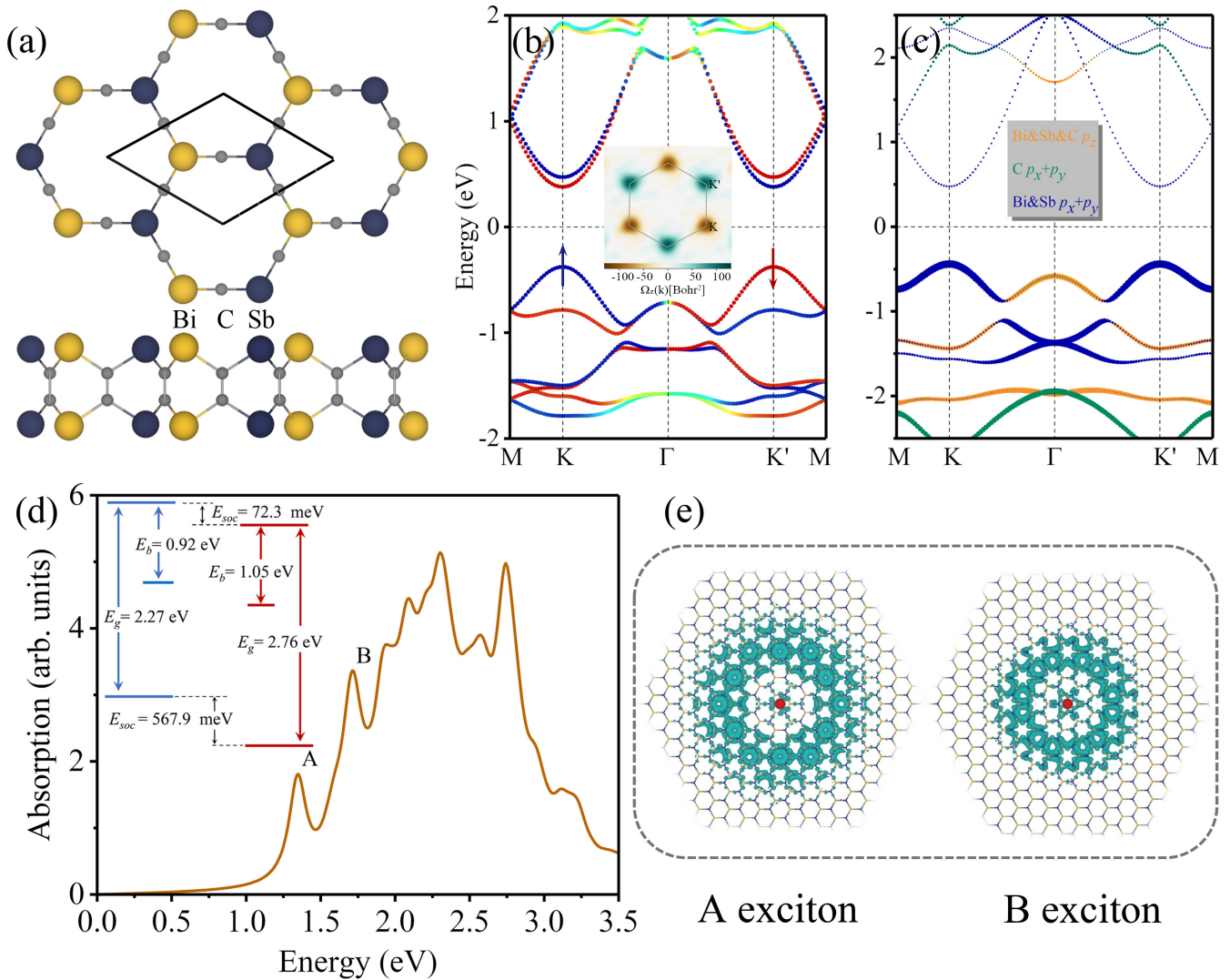


FIG. 3. (a) Top and side view of QL BiSbC₃, rhombus indicates the unit cell. (b) Spin-resolved and (c) orbital-resolved band structure, the Fermi level is set to zero. Inset to (b) is the Berry curvature of QL BiSbC₃ over the full Brillouin zone. (d) Optical absorption spectrum of QL BiSbC₃ by means of GW+Bethe-Salpeter calculations. Inset defines the relevant energy, GW quasiparticle band gap E_g , exciton binding energy E_b , SOC spin splitting E_{soc} . $E_g - E_b$ denotes the vertical optical transition energy. (e) Exciton wave functions for A and B excitons plotted with a $21 \times 21 \times 1$ supercell, red dots represent the fixed holes.

the Zeeman field, the intervalley energy degeneracy is lifted, indicative of the possibility of anomalous valley Hall effect as T breaks in XYH lattice.

In the following, we implement our theory in real material, i.e., the QL BiSbC₃ with a high group symmetry of $P\bar{6}m2$. As shown in Fig. 3(a), QL BiSbC₃ of HK lattice with interpenetrating Kagome and honeycomb lattices consists of C and M ($M = \text{Bi}$ and Sb) atoms. Its dynamical stability is verified by the phonon spectrum with positive phonon branches across the entire Brillouin zone, and the cohesive energy of -5.98 eV/atom supports the thermodynamic stability. In order to realize the XYH lattice, several methods such as adding suitable substrate and surface decoration/functionalization have been proposed according to the orbital filtering effect [34–39]. It is different from the ways mentioned above, combining the Kagome lattice consisting of C atom with honeycomb lattice of a p_z orbital can also lift the p_z orbital away

from the Fermi level; and QL BiSbC₃ which combines honeycomb and Kagome lattices could be a concrete material of this new way to achieve XYH lattice. In these strategies, $p_{x,y}$ orbitals from the honeycomb lattice are pushed to be the frontier orbitals, playing the determining role in the model. As stated below, the effective tight-binding model we constructed still works well for the discussion on the concrete material. It is different from the M_2C_3 monolayers with $P6/mmm$ symmetry [40], P breaking in QL BiSbC₃ ensures the inequality of K and K' valleys, and Zeeman-type SOC splitting appears causes the spin-valley coupling. In addition, as for 2D layered structure in absence of its parent bulk phase, a recently developed chemical vapor deposition method could enable the growth of such materials of high quality; for example, the MoSi₂N₄ [41], which was predicted by the first-principles calculations [42]. It can be expected that, therefore, theoretically predicted QL BiSbC₃ could probably be synthesized in such a way in future.

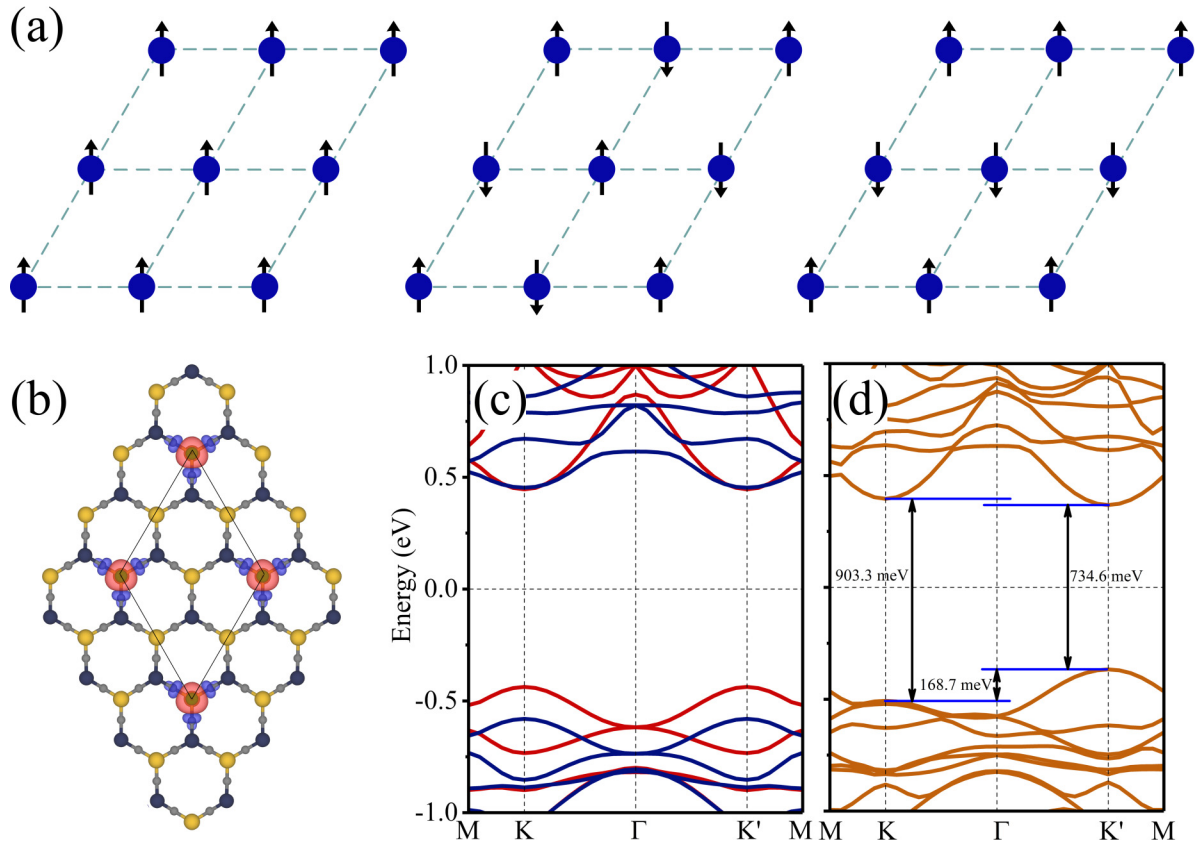


FIG. 4. (a) Sketch of possible ferromagnetic, Néel and strip antiferromagnetic spin orders in the 2D triangular lattice. (b) Spin charge density of V-doped QL BiSbC₃, where the $2 \times 2 \times 1$ supercell is indicated by a rhombus, blue and yellow isosurfaces correspond to the spin-down and spin-up states, respectively. Spin-polarized band structure of V-doped QL BiSbC₃ (c) without and (d) with SOC, the Fermi level is set to zero.

In Fig. 3(b), spin-resolved band structure illustrates direct band gaps and spin-valley coupling at the K and K' points for QL BiSbC₃. As shown in Fig. 3(c), orbital-resolved band structure reveals that band edges in K/K' valley are mainly contributed by Sb and Bi $p_{x,y}$ orbitals. It should be pointed out that C $p_{x,y}$ orbitals show a constant contribution due to the hybridization, thus can be recognized as a background state and will not be discussed due to its minor contribution to the SOC spin splitting. In case for 2D TMDCs, a similar treatment has been done [43]. It is evident that the C Kagome lattice keeps the p_z orbitals away from the K/K' valley in terms of π - π interactions, and at the same time reserves the typical electronic properties inherent to the XYH lattice, thus satisfying the requirements that we put forward in the model analysis. It is of interest that the SOC induced spin splitting for the VBM is as large as 406.9 meV (567.9 meV), while that for the CBM is 91.4 meV (72.3 meV) at PBE (GW) level of theory; increase in the contribution from C atoms is responsible for the small value for CBM.

As shown in Fig. 3(d), the large SOC spin splitting for VBM is demonstrated by the well separation of characteristic A and B excitons. As shown in the inset to Fig. 3(d), exciton binding energy is defined as the difference between the GW quasiparticle band gap and exciton transition energy that corresponds to the exciton absorption peak. In accordance to the results from the many-body perturbation theory, binding energies for spin conservative A and B excitons are

0.92 and 1.05 eV, respectively, indicative of their strongly bound nature. In Fig. 3(e), wave functions of A and B excitons offer a visual picture for the correlation of excited electrons and holes in real space. In this context, carriers of specific spin in one valley can be excited with easy control of the circularly polarized light frequency due to the large optical transition energy difference between A and B excitons (496 meV), giving rise to selective spin-photon coupling. It should be underlined that the carrier velocity with a nonzero Berry curvature can be represented as $\hbar v_n(\mathbf{k}) = \nabla_k \varepsilon_n(\mathbf{k}) - v_\perp$. ε_n corresponds to the energy of the n th Bloch band, and $\nabla_k \varepsilon_n(\mathbf{k})$ indicates the common group velocity. The transverse velocity v_\perp can be described as $v_\perp = -\frac{e}{\hbar} \mathbf{E} \times \boldsymbol{\Omega}(\mathbf{k})$, where the \mathbf{E} is the in-plane electric field and $\boldsymbol{\Omega}(\mathbf{k})$ is the Berry curvature in the out-of-plane direction, which is indispensable for the valley Hall effect. In the inset to Fig. 3(b), the valley-contrasting Berry curvature for QL BiSbC₃ over the full Brillouin zone is shown, providing the anomalous transverse velocity and thus enabling the valley Hall effect.

In case of T breaking, anomalous valley Hall effect can be another way to access and manipulate the valley degree of freedom, provided that intervalley energy degeneracy lifts; in other words, valley polarization occurs. In general, introducing magnetism such as external magnetic field, magnetic doping and magnetic proximity as well as intrinsic spontaneous valley polarization in ferrovalley materials

are usually discussed [44–52]. It is, however, still significantly challenging that the existing systems are suffering from many drawbacks, for example, the insufficient valley polarization and unacceptable in-plane magnetization; and the ferromagnetic ground state in two dimensions is even still controversial. In particular, as in many other cases, undesirable impurity states obstruct severely the utilization of the valley degree of freedom.

In respect to the QL BiSbC₃ with large on-site SOC strength, thus we speculate that obvious intervalley energy polarization will be obtained when T breaks, which is conducive to the realization of the anomalous valley Hall effect. In order to break T in QL BiSbC₃, one Bi/Sb atom in a $2 \times 2 \times 1$ supercell is replaced by a V atom with isoelectronic features. In accordance to the Stoner instability $N(E_f)I_s > 1$ [where $N(E_f)$ is the density of states (DOS) at the Fermi level and I_s is the Stoner parameter], the emergence of the magnetism can be understood. It can be deduced that criterion large DOS at the Fermi level will lead to spin splitting. In case of V-doped QL BiSbC₃ as a semiconductor with large band gap, thus applying stoner criterion maybe not a feasible way to judge the magnetic ground state, even though it has a large exchange interaction strength [53,54]. As indicated in previous studies [54–56], alternatively, it needs to calculate the energy of various magnetic orders to confirm the magnetic ground state. In the case of substituting Bi with V, as an example, the ground state is addressed by comparing the total energies of one nonmagnetic order and three possible magnetic orders, see Fig. 4(a). It is indicative that the ferromagnetic order has smaller total energy than the nonmagnetic, Néel and stripe antiferromagnetic orders. In addition, the easy axis of the ferromagnetic state is out-of-plane, 38.14 meV per cell lower than that of in-plane spin orientation by evaluating the magnetocrystalline anisotropy energy. In Fig. 4(b), spin charge density is shown, a local magnetic moment of $2.0 \mu_B$ is assigned to one V atom.

As Fig. 4(c) shows, the spin-polarized band structure of V-doped QL BiSbC₃ without SOC indicates that spin-up and spin-down channels are split significantly and the low-energy states are mainly contributed by the spin-up bands. As SOC is taken into account, the intervalley energy degeneracy is lifted and valley polarization is realized, see Fig. 4(d). In particular, the valley splitting for CBM is 28.2 meV, and for VBM is as large as 168.7 meV. In comparison to many other magnetically

doped materials, V-doped QL BiSbC₃ is featured to be a magnetic semiconductor with a clean band gap, no impurity states are introduced. It is, therefore, an indication that V doping in QL BiSbC₃ can be a promising strategy to realize the anomalous valley Hall effect. It should be emphasized that the V-doped QL BiSbC₃ is a topological trivial insulator, which is a candidate material to achieve anomalous valley Hall effect rather than an anomalous Hall effect [11,14].

IV. CONCLUSIONS

In conclusion, we proposed that $p_{x,y}$ -orbitals active honeycomb lattice (XYH lattice) harbors the valley degree of freedom with long-sought large SOC splitting based on the TB model and symmetry analysis; and the valley polarization can be detected by optical pumping by circularly polarized light and introducing a Zeeman field that breaks T . As for the material exemplification, QL BiSbC₃ can translate our proposed physics into real material. In particular, SOC splitting for QL BiSbC₃ reaches 567.9 meV (from GW approximation), and the excitonic energy difference for characteristic A and B excitons is as large as 496 meV. In contrast to many other cases, atomic V doping in QL BiSbC₃ does not introduce in-gap states obstructing the access to the valley degree of freedom. As a result of T breaking, the intervalley energy degeneracy lifts in V-doped QL BiSbC₃ with a valley polarization of 168.7 meV, indicative of a possibility to realize anomalous valley Hall effect. In closing, our work demonstrates an avenue for XYH lattice with active $p_{x,y}$ orbitals for valley physics, and identifies a concrete material for applications.

ACKNOWLEDGMENTS

This work is financially supported by the National Natural Science Foundation of China (Grants No. 51872170 and No. 12074217), the Natural Science Foundation of Shandong Province (Grant No. ZR2019MEM013), the Shandong Provincial Key Research and Development Program (Major Scientific and Technological Innovation Project) (Grant No. 2019JZZY010302), the Taishan Scholar Program of Shandong Province, and the Young Scholars Program of Shandong University (YSPSDU).

-
- [1] D. Xiao, W. Yao, and Q. Niu, *Phys. Rev. Lett.* **99**, 236809 (2007).
 - [2] K. F. Mak, K. L. McGill, J. Park, and P. L. McEuen, *Science* **344**, 1489 (2014).
 - [3] J. R. Schaibley, H. Yu, G. Clark, P. Rivera, J. S. Ross, K. L. Seyler, W. Yao, and X. Xu, *Nat. Rev. Mater.* **1**, 16055 (2016).
 - [4] W. Yao, D. Xiao, and Q. Niu, *Phys. Rev. B* **77**, 235406 (2008).
 - [5] Z. Song, Z. Li, H. Wang, X. Bai, W. Wang, H. Du, S. Liu, C. Wang, J. Han, Y. Yang *et al.*, *Nano Lett.* **17**, 2079 (2017).
 - [6] W. Feng, Y. Yao, W. Zhu, J. Zhou, W. Yao, and D. Xiao, *Phys. Rev. B* **86**, 165108 (2012).
 - [7] J. Qi *et al.*, *Phys. Rev. B* **92**, 121403(R) (2015).
 - [8] Y. Ma, L. Kou, A. Du, B. Huang, Y. Dai, and T. Heine, *Phys. Rev. B* **97**, 035444 (2018).
 - [9] T. Cao, G. Wang, W. Han, H. Ye, C. Zhu, J. Shi, Q. Niu, P. Tan, E. Wang, B. Liu *et al.*, *Nat. Commun.* **3**, 887 (2012).
 - [10] K. F. Mak, K. He, J. Shan, and T. F. Heinz, *Nat. Nanotech.* **7**, 494 (2012).
 - [11] X. Li, T. Cao, Q. Niu, J. Shi, and J. Feng, *Proc. Natl. Acad. Sci. USA* **110**, 3738 (2013).
 - [12] Z. Gong, G.-B. Liu, H. Yu, D. Xiao, X. Cui, X. Xu, and W. Yao, *Nat. Commun.* **4**, 2053 (2013).
 - [13] Y. Cheng, Q. Zhang, and U. Schwingenschlögl, *Phys. Rev. B* **89**, 155429 (2014).

- [14] H. Zeng, J. Dai, W. Yao, D. Xiao, and X. Cui, *Nat. Nanotech.* **7**, 490 (2012).
- [15] Z. Liu, F. Liu, and Y.-S. Wu, *Chin. Phys. B* **23**, 077308 (2014).
- [16] T. Zhou, J. Zhang, H. Jiang, I. Žutić, and Z. Yang, *npj Quantum Mater.* **3**, 39 (2018).
- [17] Z. Liu, W. Feng, H. Xin, Y. Gao, P. Liu, Y. Yao, H. Weng, and J. Zhao, *Mater. Horiz.* **6**, 781 (2019).
- [18] C.-C. Liu, S. Guan, Z. Song, S. A. Yang, J. Yang, and Y. Yao, *Phys. Rev. B* **90**, 085431 (2014).
- [19] Z. Liu, Z.-F. Wang, J.-W. Mei, Y.-S. Wu, and F. Liu, *Phys. Rev. Lett.* **110**, 106804 (2013).
- [20] C. Wu, D. Bergman, L. Balents, and S. Das Sarma, *Phys. Rev. Lett.* **99**, 070401 (2007).
- [21] C. Wu and S. Das Sarma, *Phys. Rev. B* **77**, 235107 (2008).
- [22] G.-F. Zhang, Y. Li, and C. Wu, *Phys. Rev. B* **90**, 075114 (2014).
- [23] X. Lu, Y. Chen, and H. Chen, *Phys. Rev. B* **101**, 195143 (2020).
- [24] W. Kohn and L. J. Sham, *Phys. Rev.* **140**, A1133 (1965).
- [25] J. P. Perdew, K. Burke, and M. Ernzerhof, *Phys. Rev. Lett.* **77**, 3865 (1996).
- [26] G. Kresse and J. Furthmüller, *Phys. Rev. B* **54**, 11169 (1996).
- [27] L. Wang, T. Maxisch, and G. Ceder, *Phys. Rev. B* **73**, 195107 (2006).
- [28] G. Pizzi Giovanni, V. Vitale, R. Arita, S. Blügel, F. Freimuth, G. Géranton, M. Gibertini, D. Gresch, C. Johnson, T. Koretsune *et al.*, *J. Phys.: Condens. Matter* **32**, 165902 (2020).
- [29] A. Togo and I. Tanaka, *Scr. Mater.* **108**, 1 (2015).
- [30] A. Marini, C. Hogan, M. Grüning, and D. Varsano, *Comput. Phys. Commun.* **180**, 1392 (2009).
- [31] P. Giannozzi, O. Andreussi, T. Brumme, O. Bunau, M. B. Nardelli, M. Calandra, R. Car, C. Cavazzoni, D. Ceresoli, M. Cococcioni *et al.*, *J. Phys.: Condens. Matter* **29**, 465901 (2017).
- [32] N. Troullier and J. L. Martins, *Phys. Rev. B* **43**, 1993 (1991).
- [33] Y. Yao, L. Kleinman, A. H. MacDonald, J. Sinova, T. Jungwirth, D.-S. Wang, E. Wang, and Q. Niu, *Phys. Rev. Lett.* **92**, 037204 (2004).
- [34] Y. Ren, Z. Qiao, and Q. Niu, *Rep. Prog. Phys.* **79**, 066501 (2016).
- [35] T. Zhou, J. Zhang, Y. Xue, B. Zhao, H. Zhang, H. Jiang, and Z. Yang, *Phys. Rev. B* **94**, 235449 (2016).
- [36] T. Zhou, S. Cheng, M. Schleenvoigt, P. Schüffelgen, H. Jiang, Z. Yang, and I. Žutić, *Phys. Rev. Lett.* **127**, 116402 (2021).
- [37] M. Zhou, W. Ming, Z. Liu, Z. Wang, P. Li, and F. Liu, *Proc. Natl. Acad. Sci. USA* **111**, 14378 (2014).
- [38] Z.-Q. Huang, F.-C. Chuang, C.-H. Hsu, Y.-T. Liu, H.-R. Chang, H. Lin, and A. Bansil, *Phys. Rev. B* **88**, 165301 (2013).
- [39] H. Zhang, Y. Wang, W. Yang, J. Zhang, X. Xu, and F. Liu, *Nano Lett.* **21**, 5828 (2021).
- [40] P.-F. Liu, T. Bo, Z. Liu, O. Eriksson, F. Wang, J. Zhao, and B.-T. Wang, *J. Mater. Chem. C* **6**, 12689 (2018).
- [41] Y.-L. Hong, Z. Liu, L. Wang, T. Zhou, W. Ma, C. Xu, S. Feng, L. Chen, M.-L. Chen, D.-M. Sun *et al.*, *Science* **369**, 670 (2020).
- [42] L. Wang, Y. Shi, M. Liu, A. Zhang, Y.-L. Hong, R. Li, Q. Gao, M. Chen, W. Ren, H.-M. Cheng, Y. Li, and X.-Q. Chen, *Nat. Commun.* **12**, 2361 (2021).
- [43] D. Xiao, G.-B. Liu, W. Feng, X. Xu, and W. Yao, *Phys. Rev. Lett.* **108**, 196802 (2012).
- [44] G. Aivazian, Z. Gong, A. M. Jones, R.-L. Chu, J. Yan, D. G. Mandrus, C. Zhang, D. Cobden, W. Yao, and X. Xu, *Nat. Phys.* **11**, 148 (2015).
- [45] Q. Zhang, S. A. Yang, W. Mi, Y. Cheng, and U. Schwingenschlögl, *Adv. Mater.* **28**, 959 (2016).
- [46] N. Singh and U. Schwingenschlögl, *Adv. Mater.* **29**, 1600970 (2017).
- [47] R. Peng, Y. Ma, S. Zhang, B. Huang, and Y. Dai, *J. Phys. Chem. Lett.* **9**, 3612 (2018).
- [48] W.-Y. Tong, S.-J. Gong, X. Wan, and C.-G. Duan, *Nat. Commun.* **7**, 13612 (2016).
- [49] P. Zhao, Y. Ma, C. Lei, H. Wang, B. Huang, and Y. Dai, *Appl. Phys. Lett.* **115**, 261605 (2019).
- [50] C. Zhang, Y. Nie, S. Sanvito, and A. Du, *Nano Lett.* **19**, 1366 (2019).
- [51] R. Peng, Y. Ma, X. Xu, Z. He, B. Huang, and Y. Dai, *Phys. Rev. B* **102**, 035412 (2020).
- [52] Y. Zang, Y. Ma, R. Peng, H. Wang, B. Huang, and Y. Dai, *Nano Res.* **14**, 834 (2021).
- [53] E. C. Stoner, *Proc. R. Soc. A* **165**, 372 (1938).
- [54] W. Jiang, H. Huang, and F. Liu, *Nat. Commun.* **10**, 2207 (2019).
- [55] J.-J. Zhang, L. Lin, Y. Zhang, M. Wu, B. I. Yakobson, and S. Dong, *J. Am. Chem. Soc.* **140**, 9768 (2018).
- [56] C. Huang, J. Feng, F. Wu, D. Ahmed, B. Huang, H. Xiang, K. Deng, and E. Kan, *J. Am. Chem. Soc.* **140**, 11519 (2018).